International Conference on Mathematics, Computational Methods & Reactor Physics (M&C 2009)
Saratoga Springs, New York, May 3-7, 2009, on CD-ROM, American Nuclear Society, LaGrange Park, IL (2009)

MODIFIED NODAL INTEGRAL METHOD INCORPORATED WITH IRREGULAR-SHAPE ELEMENTS FOR NAVIER-STOKES EQUATIONS

Kai Huang[*] and Rizwan-uddin[†]
Department of Nuclear, Plasma, & Radiological Engineering
University of Illinois at Urbana-Champaign
216 Talbot Lab, 104 S. Wright St., Urbana, IL 61801, USA
khuang21@illinois.edu; rizwan@illinois.edu

ABSTRACT

A simple isoparametric geometry mapping is applied to incorporate irregular four-node quadrilateral elements into Modified Nodal Integral Method for the two-dimensional, time-dependent, incompressible Navier-Stokes equations. The modified scheme has been applied to solve the two-dimensional lid driven cavity problem with exact solution, solved over a sub-domain that necessitate non-rectangular elements for efficient coarse discretization permitted by nodal scheme. Numerical results show that accuracy of the modified nodal integral scheme can be maintained for irregular shaped cells, thus extending the efficiency and accuracy of such schemes to domains with curved boundaries.

Key Words: Navier-Stokes; Nodal integral method; Isoparametric mapping

1. INTRODUCTION

Nodal Integral Method (NIM) for the Navier-Stokes equations was first reported by Azmy and Dorning [1]. A Modified Nodal Integral Method (MNIM) was developed for the 2D and 3D, time-dependant, Navier-Stokes equations around 2003 [2] and 2005 [3], respectively. It shows high accuracy even with relatively coarse meshes. However, the local transverse integration procedure required to obtain the set of ordinary differential equations for each cell limits the MNIM to fluid flow fields that, in 2D, can be decomposed into rectangular cells. As a result, the efficiency achieved by using coarse meshes is adversely impacted due to the need to use finer rectangular cells for problems with complex boundaries. To overcome the abovementioned restriction, a hybrid approach combining nodal integral method (NIM) and finite element method was reported earlier [4].

Recently, a simple isoparametric geometry mapping approach, which has been widely used in finite volume and finite element methods, was successfully implemented to solve the Poisson equation and the convection-diffusion equation in arbitrary domains using the NIM [5]. The results showed that accuracy of nodal integral scheme can be maintained for irregular shaped cells. The isoparametric mapping approach developed for the Poisson and convection-diffusion equations is extended here by applying the same mapping to incorporate irregular quadrilateral

[*] Corresponding author.

[†] Also, Fellow of the National Center for Supercomputing Applications, University of Illinois.

elements into MNIM for the two-dimensional, time-dependent, incompressible Navier-Stokes equations.

2. FORMULISM

2.1. Isoparametric Mapping

Consider an arbitrary quadrilateral element in spatial domain $\hat{\Omega}$, and a square element in domain Ω, as shown in Fig. 1. Notice that $\hat{\Omega}$ is characterized by global coordinates x and y, while Ω by local coordinates ξ and η with $-1 \leq \xi, \eta \leq 1$. Assume an isoparametric mapping from domain $\hat{\Omega}$ to Ω, such that $x(\xi,\eta) = [L(\xi,\eta)]\mathbf{x}$ and $y(\xi,\eta) = [L(\xi,\eta)]\mathbf{y}$ where **x** and **y** denote column vectors containing nodal values of the x and y coordinates, and the matrix $[L(\xi,\eta)] = [l_i(\xi,\eta); i = 1,2,3,4]$ has bilinear Lagrange interpolation functions (see Appendix A) as its four components. The explicit form of this linear mapping can easily be shown to be [5]

$$\begin{cases} x = \frac{(1+\xi)(1+\eta)}{4}x_1 + \frac{(1-\xi)(1+\eta)}{4}x_2 + \frac{(1-\xi)(1-\eta)}{4}x_3 + \frac{(1+\xi)(1-\eta)}{4}x_4 \\ y = \frac{(1+\xi)(1+\eta)}{4}y_1 + \frac{(1-\xi)(1+\eta)}{4}y_2 + \frac{(1-\xi)(1-\eta)}{4}y_3 + \frac{(1+\xi)(1-\eta)}{4}y_4 \end{cases} \quad (1)$$

where (x_i, y_i) indicates the i^{th} node's coordinates in global domain $\hat{\Omega}$.

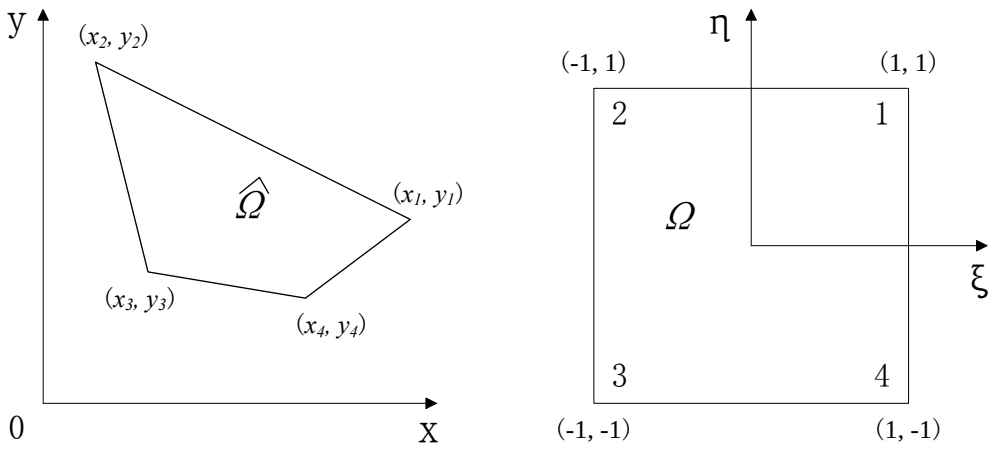

Figure 1. Mapping of the quadrilateral element to a (2×2) square element

As usual we denote by $C^0(\hat{\Omega})$ and $C^0(\Omega)$ the space of continuous functions defined over $\hat{\Omega}$ and Ω, respectively. For any continuous function $\hat{F}(x,y) \in C^0(\hat{\Omega})$, by applying mapping (1), there exists a corresponding continuous function $F(\xi,\eta) \in C^0(\Omega)$ such that [5]

$$F(\xi,\eta) = \hat{F}\big(x(\xi,\eta), y(\xi,\eta)\big) \tag{2}$$

Further, notice that mapping (1) is one-to-one and onto, which guarantees the existence of an inverse function $\hat{F}(x,y) \in C^0(\hat{\Omega})$ such that [5]

$$\hat{F}(x,y) = F\big(\xi(x,y), \eta(x,y)\big) \tag{3}$$

Moreover, if the function $\hat{F}(x,y)$ is differentiable, then its first and second order partial derivatives with respect to *x* and *y* are [4]

$$\begin{cases} \hat{F}_x = F_\xi \xi_x + F_\eta \eta_x \\ \hat{F}_y = F_\xi \xi_y + F_\eta \eta_y \end{cases} \tag{4}$$

and

$$\begin{cases} \hat{F}_{xx} = F_\xi \xi_{xx} + F_\eta \eta_{xx} + \xi_x\big(F_{\xi\xi}\xi_x + F_{\xi\eta}\eta_x\big) + \eta_x\big(F_{\eta\xi}\xi_x + F_{\eta\eta}\eta_x\big) \\ \hat{F}_{xy} = F_\xi \xi_{xy} + F_\eta \eta_{xy} + \xi_x\big(F_{\xi\xi}\xi_y + F_{\xi\eta}\eta_y\big) + \eta_x\big(F_{\eta\xi}\xi_y + F_{\eta\eta}\eta_y\big) \\ \hat{F}_{yy} = F_\xi \xi_{yy} + F_\eta \eta_{yy} + \xi_y\big(F_{\xi\xi}\xi_y + F_{\xi\eta}\eta_y\big) + \eta_y\big(F_{\eta\xi}\xi_y + F_{\eta\eta}\eta_y\big) \end{cases} \tag{5}$$

Thus, we can map an equation whose spatial variables are defined over a generic quadrilateral element in $\hat{\Omega}$ onto a target equation having spatial variables defined over a square element in domain Ω by transforming the original equation term by term using the above mapping, as long as each term represents a continuous function.

2.2. Original and Transformed Navier-Stokes Equations

The two-dimensional, time-dependent, incompressible Navier-Stokes equations in primitive variable form are

$$\begin{cases} \dfrac{\partial \hat{u}}{\partial x} + \dfrac{\partial \hat{v}}{\partial y} = 0 & (6) \\ \dfrac{\partial \hat{u}}{\partial t} + \hat{u}\dfrac{\partial \hat{u}}{\partial x} + \hat{v}\dfrac{\partial \hat{u}}{\partial y} - \nu\left(\dfrac{\partial^2 \hat{u}}{\partial x^2} + \dfrac{\partial^2 \hat{u}}{\partial y^2}\right) + \dfrac{1}{\rho}\dfrac{\partial \hat{p}}{\partial x} + \hat{b}_x = 0 & (7) \\ \dfrac{\partial \hat{v}}{\partial t} + \hat{u}\dfrac{\partial \hat{v}}{\partial x} + \hat{v}\dfrac{\partial \hat{v}}{\partial y} - \nu\left(\dfrac{\partial^2 \hat{v}}{\partial x^2} + \dfrac{\partial^2 \hat{v}}{\partial y^2}\right) + \dfrac{1}{\rho}\dfrac{\partial \hat{p}}{\partial x} + \hat{b}_y = 0 & (8) \end{cases}$$

in which *x*, *y* and *t* denote independent spatial variables and time variable respectively, while $\hat{b}_x$ and $\hat{b}_y$ represent body force terms [2]. The three dependent variables $\hat{u}$, $\hat{v}$, and $\hat{p}$ are unknowns to be solved, with hat indicating that they are defined in the global domain $\hat{\Omega}$. The continuity equation (Eq. 6) is often replaced by a Poisson type equation for the pressure variable [6], given by

$$\frac{\partial^2 \hat{p}}{\partial x^2}+\frac{\partial^2 \hat{p}}{\partial y^2}=-\rho\left(\frac{\partial \hat{u}}{\partial x}\right)^2-2\rho\frac{\partial \hat{u}}{\partial y}\frac{\partial \hat{v}}{\partial x}-\rho\left(\frac{\partial \hat{v}}{\partial y}\right)^2-\rho\frac{\partial \hat{b}_x}{\partial x}-\rho\frac{\partial \hat{b}_y}{\partial y}$$

$$-\rho\left[\frac{\partial \widehat{D}}{\partial t}+\hat{u}\frac{\partial \widehat{D}}{\partial x}+\hat{v}\frac{\partial \widehat{D}}{\partial y}-\nu\left(\frac{\partial^2 \widehat{D}}{\partial x^2}+\frac{\partial^2 \widehat{D}}{\partial y^2}\right)\right] \tag{9}$$

where the dilatation term $\widehat{D}$ is given by

$$\widehat{D}=\frac{\partial \hat{u}}{\partial x}+\frac{\partial \hat{v}}{\partial y} \tag{10}$$

Equations (7), (8) and (9) are mathematically equivalent to the original set of Navier-Stokes equations, yet have unique merit in numerical computation. For a space decomposed into arbitrary quadrilateral elements in the global domain $\hat{\Omega}$, these equations can be mapped, by applying the mapping technique introduced earlier, within each cell to another set of transformed governing equations over a square with side length of two in the local domain Ω, as follows

$$\begin{cases}
\dfrac{\partial u}{\partial t}-\nu(\xi_{xx}+\xi_{yy})\dfrac{\partial u}{\partial \xi}+\left[(\eta_x u_p+\eta_y v_p)-\nu(\eta_{xx}+\eta_{yy})\right]\dfrac{\partial u}{\partial \eta}+\xi_x u\dfrac{\partial u}{\partial \xi}+\xi_y v\dfrac{\partial u}{\partial \xi} \\
\quad +\eta_x(u-u_p)\dfrac{\partial u}{\partial \eta}+\eta_y(v-v_p)\dfrac{\partial u}{\partial \eta}-(\xi_x^2+\xi_y^2)\nu\dfrac{\partial^2 u}{\partial \xi^2}-(\eta_x^2+\eta_y^2)\nu\dfrac{\partial^2 u}{\partial \eta^2} \\
\quad -2(\xi_x\eta_x+\xi_y\eta_y)\nu\dfrac{\partial^2 u}{\partial \xi\partial \eta}+\dfrac{1}{\rho}\left(\xi_x\dfrac{\partial p}{\partial \xi}+\eta_x\dfrac{\partial p}{\partial \eta}\right)+b_1(\xi,\eta,t)=0 & (11) \\
\dfrac{\partial v}{\partial t}-\nu(\xi_{xx}+\xi_{yy})\dfrac{\partial v}{\partial \xi}+\left[(\eta_x u_p+\eta_y v_p)-\nu(\eta_{xx}+\eta_{yy})\right]\dfrac{\partial v}{\partial \eta}+\xi_x u\dfrac{\partial v}{\partial \xi}+\xi_y v\dfrac{\partial v}{\partial \xi} \\
\quad +\eta_x(u-u_p)\dfrac{\partial v}{\partial \eta}+\eta_y(v-v_p)\dfrac{\partial v}{\partial \eta}-(\xi_x^2+\xi_y^2)\nu\dfrac{\partial^2 v}{\partial \xi^2}-(\eta_x^2+\eta_y^2)\nu\dfrac{\partial^2 v}{\partial \eta^2} \\
\quad -2(\xi_x\eta_x+\xi_y\eta_y)\nu\dfrac{\partial^2 v}{\partial \xi\partial \eta}+\dfrac{1}{\rho}\left(\xi_y\dfrac{\partial p}{\partial \xi}+\eta_y\dfrac{\partial p}{\partial \eta}\right)+b_2(\xi,\eta,t)=0 & (12) \\
(\xi_x^2+\xi_y^2)\dfrac{\partial^2 p}{\partial \xi^2}+(\xi_{xx}+\xi_{yy})\dfrac{\partial p}{\partial \xi}+(\eta_x^2+\eta_y^2)\dfrac{\partial^2 p}{\partial \eta^2}+(\eta_{xx}+\eta_{yy})\dfrac{\partial p}{\partial \eta} \\
\quad +2(\xi_x\eta_x+\xi_y\eta_y)\dfrac{\partial^2 p}{\partial \xi\partial \eta}=R & (13)
\end{cases}$$

where u_p and v_p in Eqs. (11-12) represent the u and v velocities from the previous time step. The introduction of terms with u_p and v_p are intended to efficiently treat the nonlinear terms [2]. R in Eq. (13) represents the complex expression from the right hand side of Eq. (9), and will be next lumped into the pseudo-source term.

2.3. Transverse-Integration Procedure

The following local transverse-integrated ordinary differential equations are obtained after applying the *transverse integration procedure* [2] to Eqs. (11-13)

$$\begin{cases} \left[\eta_x u_p + \eta_y v_p - \nu\left(\eta_{xx} + \eta_{yy}\right)\right]\dfrac{d\bar{u}^{\xi t}(\eta)}{d\eta} - \left(\eta_x^2 + \eta_y^2\right)\nu\dfrac{d^2\bar{u}^{\xi t}(\eta)}{d\eta^2} = \bar{S}_1^{\xi t} & (14) \\ \left[\eta_x u_p + \eta_y v_p - \nu\left(\eta_{xx} + \eta_{yy}\right)\right]\dfrac{d\bar{v}^{\xi t}(\eta)}{d\eta} - \left(\eta_x^2 + \eta_y^2\right)\nu\dfrac{d^2\bar{v}^{\xi t}(\eta)}{d\eta^2} = \bar{S}_2^{\xi t} & (15) \\ \left(\eta_{xx} + \eta_{yy}\right)\dfrac{d\bar{p}^{\xi t}(\eta)}{d\eta} + \left(\eta_x^2 + \eta_y^2\right)\dfrac{d^2\bar{p}^{\xi t}(\eta)}{d\eta^2} = \bar{S}_3^{\xi t} & (16) \\ \left[\xi_x u_p + \xi_y v_p - \nu\left(\xi_{xx} + \xi_{yy}\right)\right]\dfrac{d\bar{u}^{\eta t}(\xi)}{d\xi} - \left(\xi_x^2 + \xi_y^2\right)\nu\dfrac{d^2\bar{u}^{\eta t}(\xi)}{d\xi^2} = \bar{S}_1^{\eta t} & (17) \\ \left[\xi_x u_p + \xi_y v_p - \nu\left(\xi_{xx} + \xi_{yy}\right)\right]\dfrac{d\bar{v}^{\eta t}(\xi)}{d\xi} - \left(\xi_x^2 + \xi_y^2\right)\nu\dfrac{d^2\bar{v}^{\eta t}(\xi)}{d\xi^2} = \bar{S}_2^{\eta t} & (18) \\ \left(\xi_{xx} + \xi_{yy}\right)\dfrac{d\bar{p}^{\eta t}(\xi)}{d\xi} + \left(\xi_x^2 + \xi_y^2\right)\dfrac{d^2\bar{p}^{\eta t}(\xi)}{d\xi^2} = \bar{S}_3^{\eta t} & (19) \\ \dfrac{d\bar{u}^{\xi\eta}(t)}{dt} = \bar{S}_1^{\xi\eta} & (20) \\ \dfrac{d\bar{v}^{\xi\eta}(t)}{dt} = \bar{S}_2^{\xi\eta} & (21) \end{cases}$$

where the right hand side terms are the zeroth order Legendre expansion of pseudo-source terms, and the transverse-integrated unknowns are formally defined as

$$\bar{\varphi}^{\xi t}(\eta) \equiv \frac{1}{4t_0}\int_{-t_0}^{t_0}\int_{-1}^{1}\varphi(\xi,\eta,t)\,d\xi dt\,, \qquad \varphi = u, v, p \tag{22}$$

$$\bar{\varphi}^{\eta t}(\xi) \equiv \frac{1}{4t_0}\int_{-t_0}^{t_0}\int_{-1}^{1}\varphi(\xi,\eta,t)\,d\eta dt\,, \qquad \varphi = u, v, p \tag{23}$$

$$\bar{\varphi}^{\xi\eta}(t) \equiv \frac{1}{4}\int_{-1}^{1}\int_{-1}^{1}\varphi(\xi,\eta,t)\,d\xi d\eta\,, \qquad \varphi = u, v, p \tag{24}$$

2.4. Solutions to the Local Transverse-Integrated Equations

Eqs. (14-19) and (20-21) are groups of second and first order linear ordinary differential equations, respectively. The introduction of the pseudo-source terms decouples the original set of

coupled equations and thus makes each one solvable within the local square element Ω. The solutions of Eqs. (14-19) are either of *constant+linear+exponential* form [2] or quadratic, depending on the geometry of the irregular cell specified in domain $\hat{\Omega}$; while Eqs. (20-21) have simple linear solutions.

For example, the solution of Eq. (14) is

$$\bar{u}^{\xi t}(\eta) = \frac{-\bar{S}_1^{\xi t}}{2\left(\eta_x^2 + \eta_y^2\right)\nu}\eta^2 + C_1\eta + C_2 \tag{25}$$

if $\eta_x u_p + \eta_y v_p - \nu\left(\eta_{xx} + \eta_{yy}\right) = 0$, and

$$\bar{u}^{\xi t}(\eta) = C_3 e^{\frac{\eta_x u_p + \eta_y v_p - \nu\left(\eta_{xx} + \eta_{yy}\right)}{\left(\eta_x^2 + \eta_y^2\right)\nu}\eta} + \frac{\bar{S}_1^{\xi t}\eta}{\eta_x u_p + \eta_y v_p - \nu\left(\eta_{xx} + \eta_{yy}\right)} + C_4 \tag{26}$$

if $\eta_x u_p + \eta_y v_p - \nu\left(\eta_{xx} + \eta_{yy}\right) \neq 0$.

The solution of Eq. (20) is

$$\bar{u}^{\xi\eta}(t) = \bar{S}_1^{\xi\eta}\, t + C_5 \tag{27}$$

where C_i (i=1, 2, 3, …) are arbitrary constants.

2.5. Continuity Conditions and Constraint Conditions

Following MNIM [2], continuity of 8 unknowns ($\bar{u}^{\xi t}, \bar{u}^{\eta t}, \bar{u}^{\xi\eta}, \bar{v}^{\xi t}, \bar{v}^{\eta t}, \bar{v}^{\xi\eta}, \bar{p}^{\xi t}, \bar{p}^{\eta t}$) and their derivatives on interface of neighboring elements are imposed to obtain a set of 16 discrete algebraic equations containing 8 unknown pseudo-source terms. Constraint conditions are then applied to eliminate the pseudo-source terms [1]. Three of the eight constraint conditions are obtained by ensuring that Eqs. (14-21) can be satisfied within each element in an integral sense, by operating both sides of these equations with $\frac{1}{8t_0}\int_{-t_0}^{t_0}\int_{-1}^{1}\int_{-1}^{1} d\xi d\eta dt$. The requirement for the uniqueness of the transverse-integrated unknowns leads to the other five constraint conditions [1, 2]. For example,

$$\bar{u}^{\xi t\eta} = \frac{1}{2}\int_{-1}^{1}\bar{u}^{\xi t}(\eta)\, d\eta = \frac{1}{2t_0}\int_{-t_0}^{t_0}\bar{u}^{\xi\eta}(t)\, dt = \bar{u}^{\xi\eta t} \tag{28}$$

The final set of 8 discrete algebraic equations for the 8 surface- or element-averaged unknowns are then obtained after eliminating the pseudo-source terms by applying the constraint equations.

The set of discrete algebraic equations are then solved iteratively, using Gauss-Seidel iterative procedure in conjunction with a SIMPLE-like algorithm [2].

3. NUMERICAL RESULTS AND DISCUSSION

In this section, a variation of the classical lid driven cavity problem—the *modified lid driven cavity problem* [7, 2]—is discussed. This problem was first proposed by Shin el al. [7], and it has an exact analytic solution with a prescribed lid velocity as well as an artificial body force term. Exact solution for both the velocity and pressure field of the modified lid driven cavity problem is respectively given by [7]

$$u(x,y) = 8(x^2 - 2x^3 + x^4)(-2y + 4y^3) \tag{29}$$

$$v(x,y) = -8(2x - 6x^2 + 4x^3)(-y^2 + y^4) \tag{30}$$

$$p(x,y,Re) = \frac{8}{Re}\left(24\left(\frac{x^3}{3} - \frac{x^4}{2} + \frac{x^5}{5}\right)y + (2x - 6x^2 + 4x^3)(-2y + 4y^3)\right) + 64\left(\frac{x^4}{2} - 2x^5 + 3x^6 - 2x^7 + \frac{x^8}{2}\right)(-(-2y + 4y^3)^2 + (-2 + 12y^2)(-y^2 + y^4)) \tag{31}$$

where *Re* denotes to the Reynolds number. Note that the lid velocity is given by

$$u_{lid}(x) = u(x, y = 1) = 16(x^2 - 2x^3 + x^4) \tag{32}$$

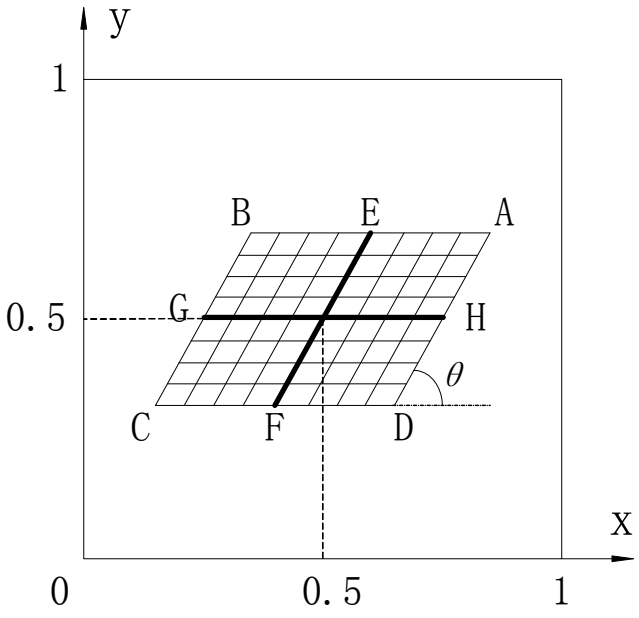

Figure 2. Schematic diagram for the modified lid-driven cavity problem

The new implementation of MNIM developed earlier in this paper is tested by calculating the velocity and pressure field over a parallelogram within the unit cavity. The parallelogram *ABCD*, shown in Fig. 2, is centered in the cavity, with a uniform edge length of 0.5. It can deform continuously as the angle θ measured between the edge *AD* and the horizontal line is changed continuously. Simulations are carried out for three θ values—$\frac{5\pi}{12}, \frac{\pi}{3}, \frac{\pi}{4}$. Dirichlet boundary conditions are imposed upon the four external edges of the parallelogram *ABCD* using the exact solutions given in Eqs. (29-31). Though exact edge-averaged values can be evaluated and specified as boundary conditions, results reported below are evaluated using the point values at the center of the edge as boundary conditions. The time-independent, modified lid driven cavity problem can be solved by marching in time from an arbitrary initial condition (both the velocity and pressure fields are set uniformly to zero as the initial condition in this work) till steady state is achieved [2]. Numerical results reported below are for Reynolds number *Re* = 1. Note that the velocity field in this *manufactured* problem is not affected by the Reynolds number. The numerical results showed very good agreement with exact solution for all eight unknowns in this problem. As an example, Fig. 3 shows qualitative comparison between exact and numerical solutions for $\bar{u}^{\xi\eta}$ and $\bar{p}^{\eta t}$ (8×8 mesh, $\theta = \frac{\pi}{4}$). The *x*- and the *y*-axis in the figure indicate the edge number along boundaries of the parallelogram *ABCD*.

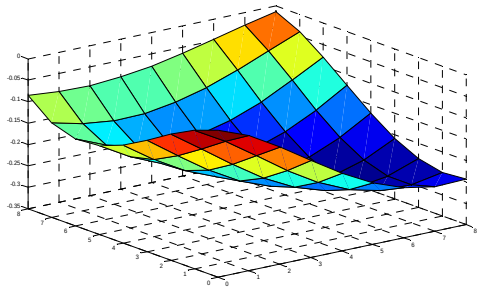

Figure 3a. Exact solution for $\bar{u}^{\xi\eta}$

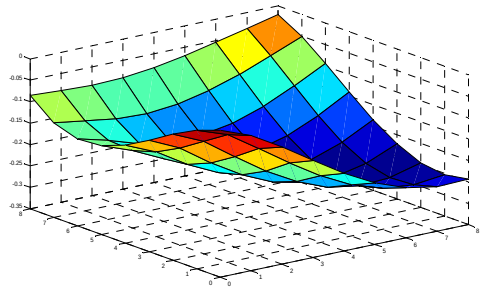

Figure 3b. Numerical solution for $\bar{u}^{\xi\eta}$

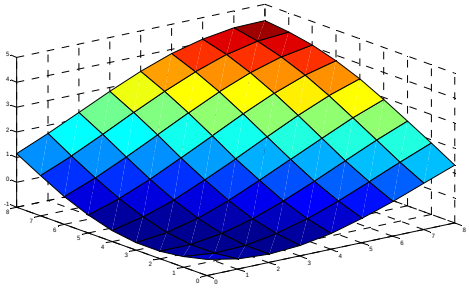

Figure 3c. Exact solution for $\bar{p}^{\eta t}$

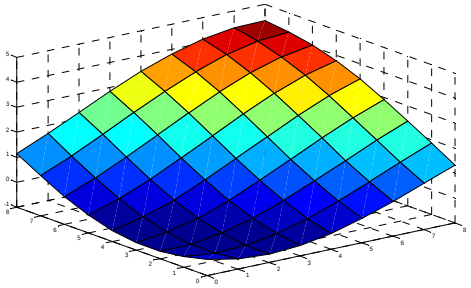

Figure 3d. Numerical solution for $\bar{p}^{\eta t}$

Figure 3. Global comparison of exact and numerical solutions for $\bar{u}^{\xi\eta}$ and $\bar{p}^{\eta t}$. (8×8 mesh, $\theta = \frac{\pi}{4}$)

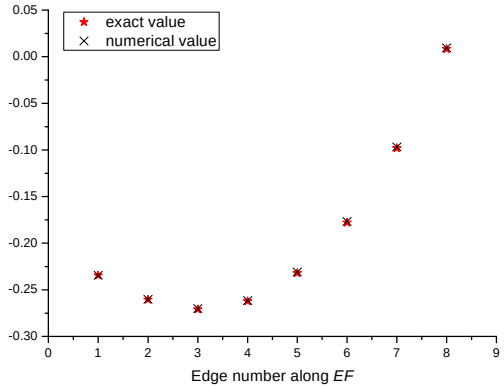

Figure 4a. $\bar{u}^{\eta t}$values along *EF* (8×8 mesh, $\theta = \frac{5\pi}{12}$)

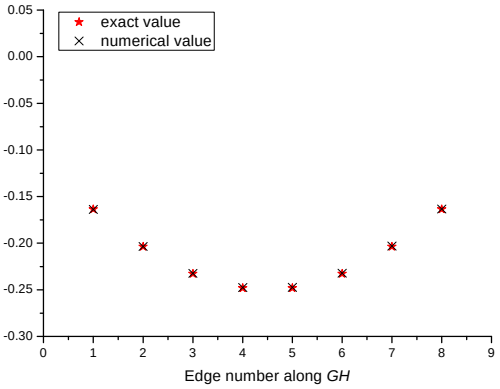

Figure 4b. $\bar{u}^{\xi t}$values along *GH* (8×8 mesh, $\theta = \frac{5\pi}{12}$)

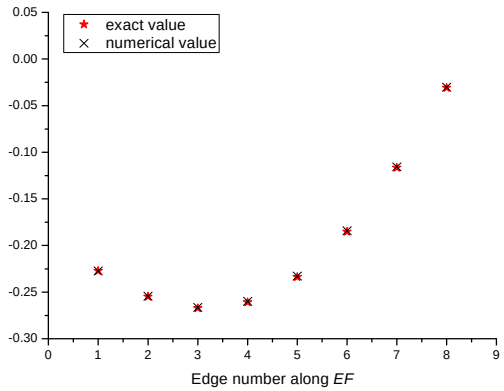

Figure 4c. $\bar{u}^{\eta t}$values along *EF* (8×8 mesh, $\theta = \frac{\pi}{3}$)

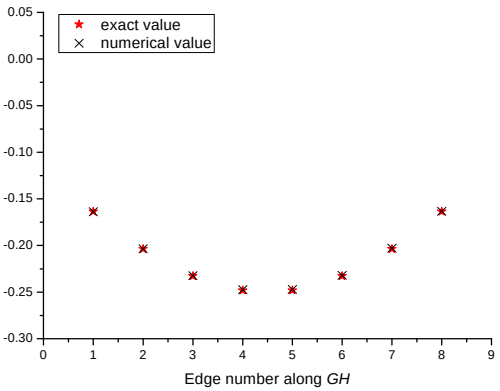

Figure 4d. $\bar{u}^{\xi t}$values along *GH* (8×8 mesh, $\theta = \frac{\pi}{3}$)

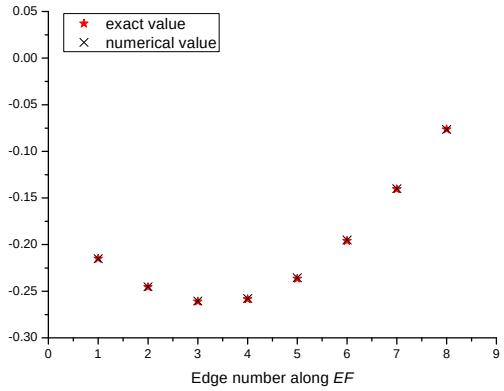

Figure 4e. $\bar{u}^{\eta t}$values along *EF* (8×8 mesh, $\theta = \frac{\pi}{4}$)

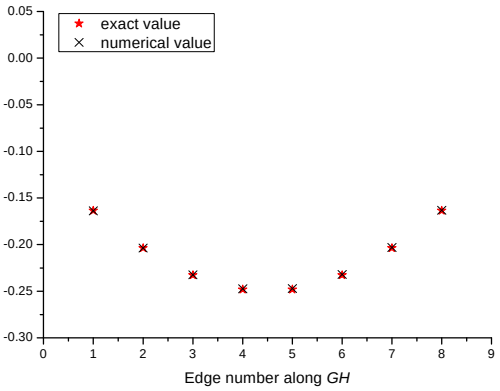

Figure 4f. $\bar{u}^{\xi t}$values along *GH* (8×8 mesh, $\theta = \frac{\pi}{4}$)

Figure 4. Comparison of exact and numerical solutions along lines *EF* and *GH*. Results are for 8×8 mesh, for three different values of θ ($= \frac{5\pi}{12}, \frac{\pi}{3}, \frac{\pi}{4}$).

Figure 4 shows the numerical edge-averaged u velocities $\bar{u}^{\eta t}$ and $\bar{u}^{\xi t}$ along the two lines EF and GH (as shown in Fig. 2) respectively for three θ values (8×8 mesh, $\theta = \frac{5\pi}{12}, \frac{\pi}{3}, \frac{\pi}{4}$). Points E, F, G and H bisect edges AB, CD, BC and AD, respectively. Also shown in Fig. 4 are the exact values of u at the center of the edge for comparison.

RMS errors in $\bar{u}^{\xi t}$, $\bar{v}^{\eta t}$, $\bar{p}^{\xi t}$,and $\bar{p}^{\eta t}$are reported for different mesh sizes as well as different θ values in Tables I-III. Mesh refinement study shows that the scheme is of second order. Moreover, as the elements are distorted from $\theta = \frac{5\pi}{12}$ to $\theta = \frac{\pi}{4}$, there is no significant increase in the RMS errors.

Table I. RMS errors for $\theta = 5\pi/12$

Mesh	$\bar{u}^{\xi t}$	$\bar{v}^{\eta t}$	$\bar{p}^{\xi t}$	$\bar{p}^{\eta t}$
4×4	0.28364×10^{-1}	0.79798×10^{-2}	0.96540×10^{-2}	0.52180×10^{-2}
8×8	0.63235×10^{-2}	0.35691×10^{-2}	0.22393×10^{-2}	0.12492×10^{-2}
16×16	0.14737×10^{-2}	0.16972×10^{-2}	0.52121×10^{-3}	0.29883×10^{-3}

Table II. RMS errors for $\theta = \pi/3$

Mesh	$\bar{u}^{\xi t}$	$\bar{v}^{\eta t}$	$\bar{p}^{\xi t}$	$\bar{p}^{\eta t}$
4×4	0.29686×10^{-1}	0.12550×10^{-1}	0.10575×10^{-1}	0.71241×10^{-2}
8×8	0.65353×10^{-2}	0.56231×10^{-2}	0.23918×10^{-2}	0.16714×10^{-2}
16×16	0.15072×10^{-2}	0.26725×10^{-2}	0.54520×10^{-3}	0.39126×10^{-3}

Table III. RMS errors for $\theta = \pi/4$

Mesh	$\bar{u}^{\xi t}$	$\bar{v}^{\eta t}$	$\bar{p}^{\xi t}$	$\bar{p}^{\eta t}$
4×4	0.28833×10^{-1}	0.12162×10^{-1}	0.99758×10^{-2}	0.72032×10^{-2}
8×8	0.63403×10^{-2}	0.54619×10^{-2}	0.22512×10^{-2}	0.16932×10^{-2}
16×16	0.14693×10^{-2}	0.25943×10^{-2}	0.51814×10^{-3}	0.39555×10^{-3}

4. CONCLUSIONS

Using a simple isoparametric geometry mapping and thus transforming irregular four-node quadrilateral elements into square elements, the modified nodal integral scheme is applied to the transformed Navier-Stokes equations. This approach has often been used in finite volume and finite element schemes. While the transformation of the quadrilateral elements to square elements is straight forward, the transformed set of the momentum equations are significantly more complicated, including additional nonlinear convective terms; linear convective terms; linear combination of pressure gradients in the two directions; as well as mixed derivative terms similar to the diffusion term (Eqs. (11-12)). The transformed pressure equation is more complicated as

well, with additional terms including the convection-like first derivative terms with constant coefficients. The appearance of the additional terms can be explained based on physical grounds. No approximations are introduced in the transformation of the element and the governing equations from (x, y) to (ξ, η) space.

The modified scheme is applied to solve the two-dimensional lid driven cavity problem with exact solution, solved over a sub-domain that necessitate non-rectangular elements for efficient coarse discretization permitted by the nodal scheme. Numerical results show that accuracy of the modified nodal integral scheme can be maintained for irregular shaped cells, thus extending the efficiency and accuracy of such schemes to domains with curved boundaries. Though RMS errors are small, they may decrease even more once the averaged values calculated numerically are compared with averaged values from the exact solution (rather than the point values).

Mesh refinement (Tables I-III) show that the scheme is of second order for edge averaged values ($\bar{u}^{\xi t}$, $\bar{p}^{\eta t}$, etc). The RMS errors do not increase significantly for the problem studied as the element distortion was increased over a limited range ($\frac{\pi}{4} \leq \theta < \frac{\pi}{2}$).

Approximations introduced in the development of the numerical scheme are similar to those made in conventional nodal schemes. One additional approximation made is that the mixed derivative terms (see Eqs. (11-13)) $\frac{\partial^2 u}{\partial \xi \partial \eta}$, $\frac{\partial^2 v}{\partial \xi \partial \eta}$ and $\frac{\partial^2 p}{\partial \xi \partial \eta}$ also need to be approximated as they lead to corner values in the final set of discrete equations. A logical extension of the work reported here is to use more general, rather than linear, mapping to allow more accurate representation of elements with curved boundaries in the transformed space.

ACKNOWLEDGMENTS

Research funded in part by the National Center for Supercomputing Applications (NCSA)/University of Illinois Faculty Fellows Program.

REFERENCES

1. Y.Y. Azmy, J.J. Dorning, "A Nodal Integral Approach to the Numerical Solution of Partial Differential Equations," *in Advances in Reactor Computations*, American Nuclear Society, LaGrange Park, IL, 1983, Vol. II, pp.893-909 (1983).
2. F. Wang and Rizwan-uddin, "A Modified Nodal Scheme for the Time-Dependent, Incompressible Navier-Stokes Equations," *Journal of Computational Physics*, **187**, pp.168-196 (2003).
3. F. Wang and Rizwan-uddin, "Modified Nodal Integral Method for the Three-Dimensional, Time-Dependent, Incompressible Navier-Stokes Equations," *Nuclear Science and Engineering*, **187**, pp.107-114 (2005).
4. A.J. Toreja and Rizwan-uddin. "Hybrid Numerical Methods for Convection-Diffusion Problems in Arbitrary Geometries," *Computers & Fluids*, **32(6)**, pp.835-872 (2003).
5. E.G. Nezami, S. Singh, N. Sobh and Rizwan-uddin, "A Nodal Integral Method for Quadrilateral Elements," *International Journal for Numerical Methods in Fluids*, DOI: 10.1002/fld.1949 (2008).

6. J.C. Tannehill, D.A. Anderson, R.H. Pletcher, *Computational Fluid Mechanics and Heat Transfer (second ed.)*, Taylor & Francis (1997).
7. T.M. Shin, C.H. Tan, B.C. Hwang, "Effects of Grid Staggering on Numerical Schemes," *International Journal for Numerical Methods in Fluids*, **9**, pp.193-212 (1989).

APPENDIX A

Bilinear Lagrange interpolation functions for two-dimensional, 4-node interpolation is given by

$$l_i(\xi,\eta) = \prod_{\substack{j=1 \\ j\neq i}}^{4} \prod_{\substack{k=1 \\ k\neq i}}^{4} \frac{(\xi - \xi_j)(\eta - \eta_k)}{(\xi_i - \xi_j)(\eta_i - \eta_k)} \quad (i = 1,2,3,4) \tag{A}$$

where ξ_i and η_i indicate the nodal values of the i^{th} node's ξ and η coordinates.